



Centimeter-scale wide-field-of-view laser-scanning photoacoustic microscopy for subcutaneous microvasculature *in vivo*

TANGYUN LIAO,^{1,4} YUAN LIU,^{1,4} JUNWEI WU,^{1,2} LIJUN DENG,^{1,3} YU DENG,² LVMING ZENG,^{1,3,*} AND XUANRONG JI¹

¹State Key Laboratory of Precision Electronics Manufacturing Technology and Equipment, Guangdong University of Technology, Guangzhou 510006, China

²Doppler Electronic Technologies Incorporated Company, Guangzhou 510530, China

³Key Lab of Optic-Electronic and Communication, Jiangxi Science and Technology Normal University, Nanchang 330038, China

⁴T. Liao and Y. Liu contributed equally to this work

*zenglvming@163.com

Abstract: We developed a simple and compact laser-scanning photoacoustic microscopy (PAM) for imaging large areas of subcutaneous microvasculature *in vivo*. The reflection-mode PAM not only retains the advantage of high scanning speed for optical scanning, but also offers an imaging field-of-view (FOV) up to $20 \times 20 \text{ mm}^2$, which is the largest FOV available in laser-scanning models so far. The lateral resolution of the PAM system was measured to be $17.5 \text{ }\mu\text{m}$. Image experiments on subcutaneous microvasculature in *in vivo* mouse ears and abdomen demonstrate the system's potential for fast and high-resolution imaging for injuries and diseases of large tissues and organs.

© 2021 Optical Society of America under the terms of the [OSA Open Access Publishing Agreement](#)

1. Introduction

Photoacoustic microscopy (PAM) is an emerging hybrid biomedical imaging technique for subcutaneous blood-bearing structures with rich optical contrast, high spatial resolution, and sufficient imaging depth [1–3], and has shown wide applications in the field of vascular biology [4–6], oncology [7–9], and ophthalmology [10–12]. Based on different configurations of optical excitation and acoustic detection, PAM can be classified into acoustic resolution photoacoustic microscopy (AR-PAM) [13–15] and optical-resolution photoacoustic microscopy (OR-PAM) [16–18]. Typically, AR-PAM systems using dark-field illumination mode to achieve the coaxial alignment of the transducer and the illumination beam [19,20]. The laser beam first formed into a ring shape illumination by a spherical conical lens to bypass the focused ultrasound transducers positioned directly below it, and then be weakly focused into the tissue by a lampshade optical condenser, with the focal region coaxially overlapping the focus of the transducer [21]. Although AR-PAM can overcome the limit of optical diffusion to provide a deeper penetration depth in biological tissues [21], its lateral resolution (typically tens to hundreds of micrometers) is not sufficient to distinguish microvasculature structures, and AR-PAM can only be used with conventional mechanical scanning which resulting in a bulky system and slow scanning speed. In contrast, OR-PAM allows optical diffraction-limited lateral resolution with a tightly focused laser spot excitation by using a high numerical aperture (NA) optical objective lens. OR-PAM systems usually used a customized optical-acoustic combiner for redirecting acoustic waves to coaxially align the optical and acoustic beams [22,23]. There are also some optional ways to achieve optical-acoustic coaxial alignment, such as using a customized ring-shaped transducer with a central hole to pass the focused beam [24] or using a reflective dark-field optical objective that allows the beam to bypass the transducer and be focused underneath it [25].

It can be found that due to the opacity of the traditional ultrasound transducers, these above-mentioned traditional PAMs usually require additional methods to achieve the coaxial alignment of optical excitation and acoustic detection paths, including the use of dark-field illumination, customized optical-acoustic combiner, and customized ring-shaped transducer. Besides, these traditional PAMs have an inevitable trade-off between imaging speed and field of view (FOV): mechanical scanning mode means low imaging speed and optical scanning mode means small FOV as low as a few millimeters. Although optical scans can be used instead of low-speed mechanical scans to dramatically increase imaging speed by a two-dimensional (2D) galvanometer, the FOV was still limited to no more than 100 μm [26,27]. This is because the acoustic beam cannot be scanned by the same mirrors in the air, so the focused laser beam can only be scanned in the acoustic focus area of the transducer. Some off-axis PAMs relax the FOV to 6 mm at the cost of approximately 40 dB loss of acoustic detection sensitivity by placing an unfocused ultrasound transducer on the off-axis position of an excitation beam [11,18]. By mounting the entire imaging head on a voice coil scanner, PAMs can also increase the scanning range to a few millimeters with 40 Hz scanning speed, without sensitivity loss [28–30]. However, the voice-coil scanner is bulky and its speed is limited by the mass of the imaging head. Recently, a water-immersible microelectromechanical system (MEMS) scanning mirror was applied to the PAM system [31,32], where the whole waterproof MEMS scanning system was immersed in water and simultaneously scanned the laser and acoustic beams. Although it can widen the imaging FOV to 3 mm while maintaining coaxial alignment and high imaging speed, such a water-immersible MEMS scanner is expensive and not widely available. So far, the FOV of optical scanning PAMs is still limited to a few millimeters which are hard enough to meet the future high-resolution imaging needs of large tissue and organs, such as limbs [33], breasts [34], and whole-brain [35], etc. Therefore, achieving fast imaging over a wider FOV remains as yet challenging for PAM.

The emergence of the transparent ultrasound transducer offers a simple solution to the coaxial alignment problem of optical illumination and acoustic detection, which have been used in PAM with a less than 10 mm FOV and low-speed mechanical scans [36–40]. In this letter, we present a centimeter-scale FOV laser-scanning PAM with a 33 mm \times 33 mm external size LiNbO₃ based transparent ultrasound transducer and a 2D scanning galvanometer, which not only has the properties of being inexpensive, simple, and compact, but also achieved the fast high-resolution imaging over a large area of 20 \times 20 mm². PAM imaging performance is evaluated by imaging the phantom (carbon-fibers, ink capillaries, and leaf vein skeletons) and the biological tissue (subcutaneous microvasculature of the *in-vivo* mouse ears and abdominal).

2. Materials and methods

LiNbO₃ single crystal exhibits a great electromechanical coupling coefficient and is easily processed by high-temperature sputtering without loss of polarization [41], making it an ideal candidate for transparent ultrasound transducers [42–44]. Figure 1(a) shows the cross-sectional schematic view of the transparent ultrasound transducer. A 36° rotated Y-cut LiNbO₃ wafer was diced into square pieces of 20 \times 20 mm² and then was processed to 365 μm thickness. 200 nm thick transparent indium tin oxide (ITO) electrodes were sputtered on both sides of the LiNbO₃ wafer and connected to the BNC connector by two micro-silver wires. A square metal housing was placed concentrically with the LiNbO₃ wafer and then pour the non-conductive epoxy into the gap between the wafer and housing. Finally, a 66 μm thick layer of optically transparent epoxy (EPO-TEK 301-2) was vapor-deposited onto the top surface of the transducer as the matching layer. A photograph of the fabricated transparent ultrasound transducer on the top of a coordinate paper is shown in Fig. 1(b). Figure 1(c) shows the transmittance of the LiNbO₃ wafer and the fabricated transparent ultrasound transducer. The transmittance curve of the fabricated transparent ultrasound transducer shows a peak of 73.05% at 512 nm and coincides with the

transmittance curve of the LiNbO_3 wafer. Due to the transducer's transmittance of 532 nm wavelength light is 72.65%, which is very close to its maximum transmittance, and considering the existing conditions in our laboratory, a 532 nm laser was finally chosen as the light source for the PAM system. The electromechanical coupling coefficient (K_{eff}) is an important parameter to evaluate the performance of the transparent ultrasound transducer which can be calculated by the resonance frequency (f_r) and anti-resonance frequency (f_a) of the transducer. As can be seen in the measured impedance spectra (Fig. 1(d)), the f_r and f_a were measured to be 8.9 MHz and 10.3 MHz, respectively, and the K_{eff} of the transparent ultrasound transducer can be calculated as 0.62. Meanwhile, the pulse-echo measurement results of the transparent ultrasound transducer showed a center frequency of 10 MHz and a -6 dB fractional bandwidth of 16.46%, as seen in Fig. 1(e). The reason for the slightly lower bandwidth is due to the absence of a backing layer for our transparent transducers, which can be improved by adding a backing layer with high acoustic

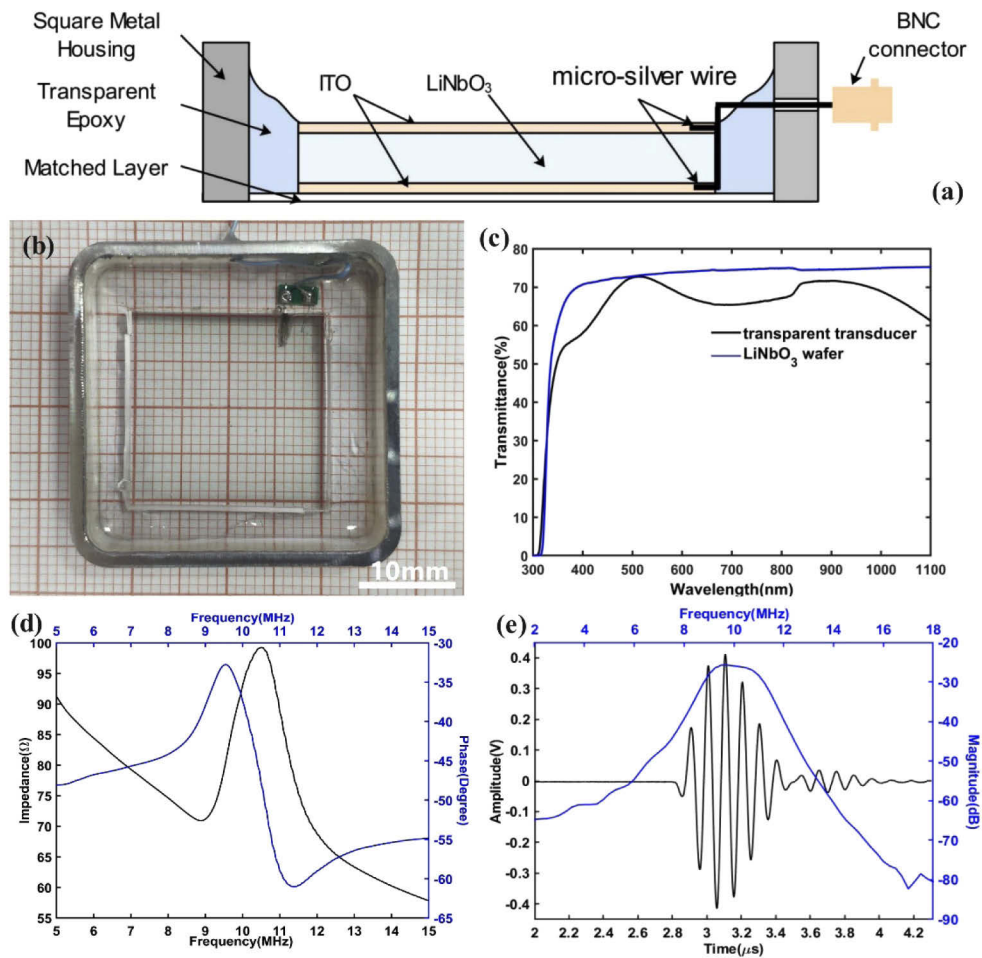


Fig. 1. (a) The cross-sectional schematic view of the transparent ultrasound transducer. ITO: Indium tin oxide. (b) Photograph of a fabricated transparent ultrasound transducer with external size of $33 \times 33 \text{ mm}^2$. (c) Light transmittance curves of the LiNbO_3 wafer and the fabricated transparent ultrasound transducer. (d) Measured electrical impedance and phase angle of the transducer. (e) Pulse-echo response curve of the transducer and its frequency spectrum.

absorption and high light transmission as well as optimizing the impedance matching layer. The theoretical axial resolution of the PAM system can be calculated as $782.5\ \mu\text{m}$ according to the bandwidth.

A schematic diagram of the simple PAM system setup is shown in Fig. 2(a). A Nd:YAG laser (PR-532-8-A, 532 nm, Power-Laser Inc.) with a wavelength of 532 nm, a pulse width of 10 ns, and a repetition frequency of 5 kHz was used as the light source. The output laser beam was reshaped to about 1.5 mm in diameter by an iris and then expanded to about 6.0 mm by a beam expander, which consists of a biconvex lens ($f = 30\ \text{mm}$, L1) and a plano-convex lens ($f = 120\ \text{mm}$, L2). After focusing by a fast electrically tunable lens (EL-10-30-Ci-VIS-LD, Optotune Inc.), the laser beam was steered by a two-dimensional (2D) scanning galvanometer (GVS002, Thorlabs Inc.) to raster-scan the sample with lower focal spot distortion. The focused laser passed through the transparent ultrasound transducer and delivered to the imaging objectives. The transducer was embedded in a bottom of the water tank, which has an imaging window on the top, sealed with a thin polyethylene film. The distance between the transducer and the focal plane was fixed at 14 mm by the customized water tank. The excited photoacoustic signal was detected by the whole aperture area of the transducer, which is then amplified by a signal amplifier (Olympus, 54 dB) and digitized by a high-speed data acquisition (DAQ) card (10bit, PXIe 5160, NI) at a sampling rate of 100 MS/s. During the actual imaging experiment, we averaged the photoacoustic signal 6 times, and considering the 5 kHz laser repetition frequency, the imaging speed of the PAM system can reach 833 pixels per second. Assuming a $20\ \mu\text{m}$ scan step, the system can achieve an imaging speed of 100 Hz/mm without considering the signal averaging. The triggering of the laser and data acquisition, as well as the scanning of the galvanometer, were controlled by an analog voltage output card (NI-9263, NI, $\pm 10\ \text{V}$, 100 KS/s). Figure 2(b) and (c) showed the photograph of our PAM system and the top view of the imaging head, respectively.

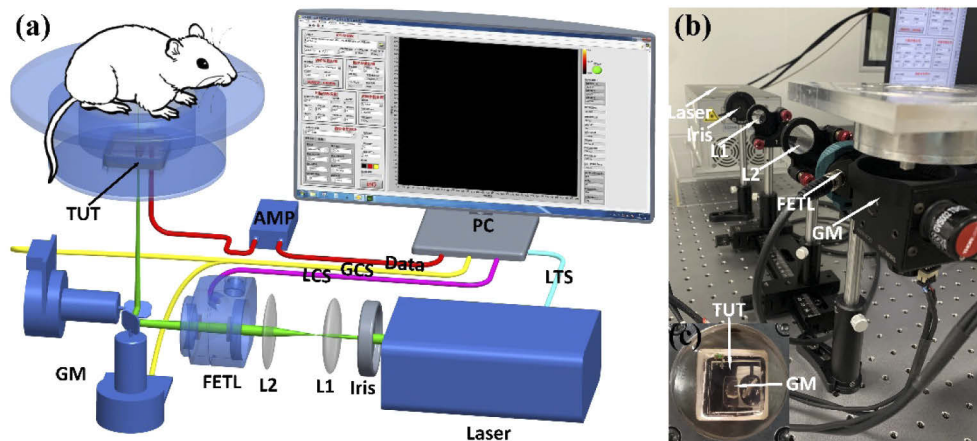


Fig. 2. (a) Schematic diagram of the simple PAM system setup (FETL, fast electrically tunable lens; GM, galvanometer; AMP, amplifier; LCS, lens control signal; GCS, galvanometer control signal; LTS, laser trigger signal). (b) Photograph of the PAM system. (c) Top view of the PAM system imaging window.

3. Result

3.1. System characterization

In our experimental conditions, the theoretical laser spot size limit of the FETL was calculated as about $16\ \mu\text{m}$, which could be considered as the theoretical lateral resolution of the PAM system. To evaluate the actual lateral resolution, we performed the imaging experiments on a 10×10

mm² range of carbon-fiber network with a diameter of about 7 μ m, as shown in Fig. 3(a). The maximum amplitude projection (MAP) image of the large range carbon-fiber network was shown in Fig. 3(b), from which each carbon fiber filament can be clearly distinguished. The MAP image of the small range carbon-fiber network marked by the white dashed box in Fig. 3(b) was shown in Fig. 3(c) and the cross-sectional profile along the dashed line marked therein was shown in Fig. 3(d). The edge expansion function ([ESF], blue line) was estimated by fitting the edge response ([Data], black dots), and the line expansion function ([LSF], red line) was obtained by calculating the first derivative of the fitted ESF curve. According to the full-width-half-height (FWHM), the lateral resolution of the PAM system was estimated to be 17.5 μ m.

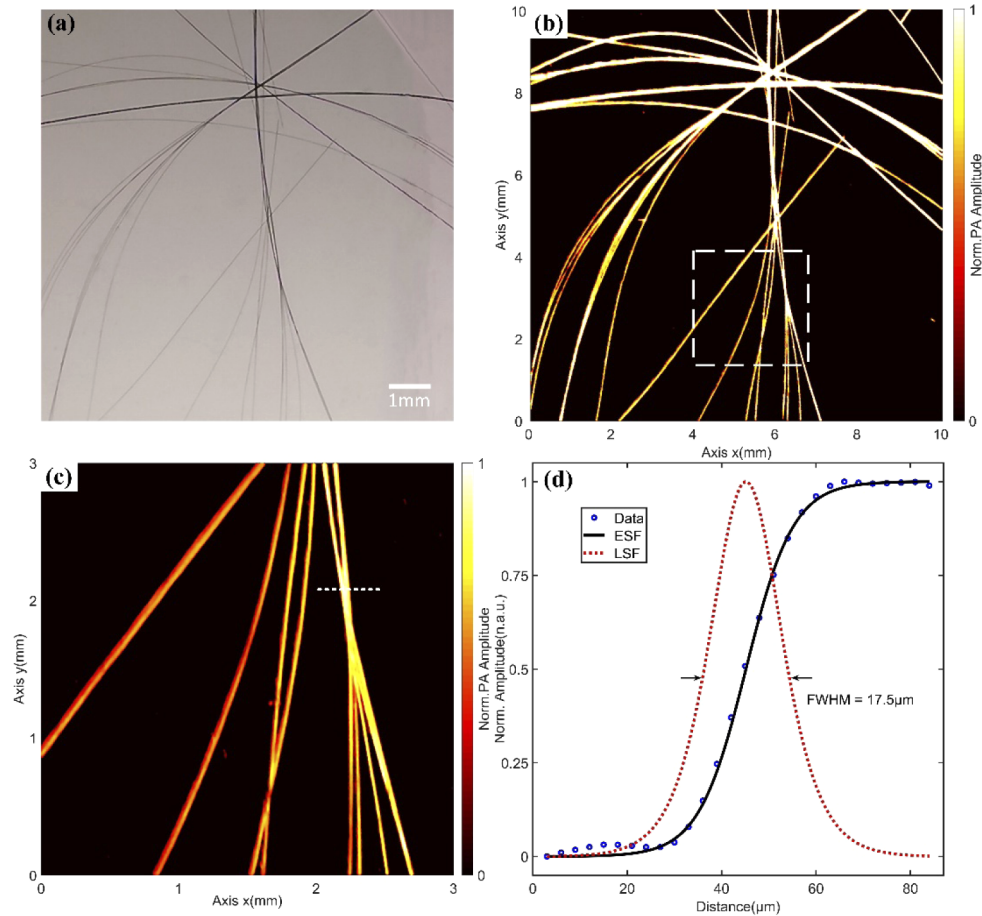


Fig. 3. (a) Photograph of the carbon fiber network. (b) MAP image of the carbon-fiber network with 10 × 10 mm² area. (c) The close-up MAP image in the area indicated by a box in (b). (d) Measurement of the lateral resolution of the PAM system (the lateral resolution was measured to be 17.5 μ m; ESF, edge expansion function; LSF, line expansion function).

3.2. Phantom imaging experiments

We performed imaging experiments on a large size range of ink capillaries and leaf vein skeletons to verify the FOV of the PAM system. In the imaging experiments on the ink capillaries, the diameter of the ink capillary was 300 μ m, and a step size of 30 μ m was used to scan a range of a 20 × 20 mm² area, which was equivalent to the area size of the transmissive window of the

transparent ultrasound transducer. The optical picture and MAP image of the ink capillaries were shown in Fig. 4(a) and Fig. 4(b), respectively. Each of the ink capillaries can be clearly distinguished in the figure, and the diameter of the ink capillaries shown in the photoacoustic image matched its actual diameter. Next, we performed a $20 \times 20 \text{ mm}^2$ large area scan imaging on a leaf vein skeleton, and its wide-field optical microscopy image was shown in Fig. 4(c). Considering the tiny branch diameter of the skeleton, the scanning step was set to $15 \mu\text{m}$. The MAP image of the leaf vein skeleton was shown in Fig. 4(d), from which the tiny branching structures in the skeleton can be clearly distinguished with adequate resolution and contrast. The absence of the photoacoustic signal in the area marked in the MAP image was due to the metal electrode in the transmissive window of the transparent transducer blocking the path of the laser beam. The imaging experiments on the two phantom samples verified that the PAM system had a large imaging FOV of $20 \times 20 \text{ mm}^2$ and could image samples in the centimeter range.

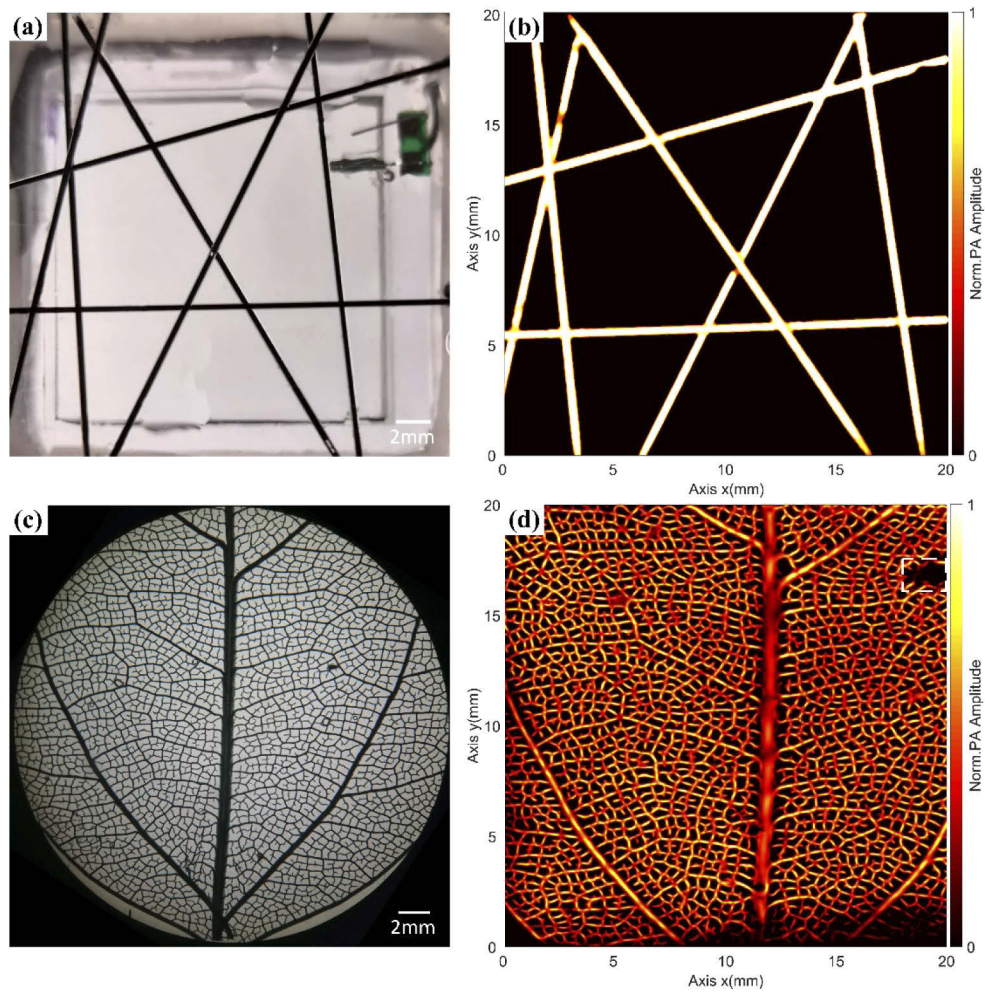


Fig. 4. (a) Photograph of the ink capillaries on the imaging window of the transparent ultrasound transducer. (b) MAP image of the ink capillaries with $20 \times 20 \text{ mm}^2$ area. (c) The wide-field optical microscopy image of the leaf vein skeleton. (d) MAP image of the leaf vein skeleton with $20 \times 20 \text{ mm}^2$ area.

3.3. Biological tissue imaging experiments

To verify the PAM system's ability to image the subcutaneous microvasculature networks, we performed a scan imaging experiment on *in vivo* mouse (Kunming mice) ears. The optical photograph of the mouse ear was shown in Fig. 5(a), from which only a few large aortic vessels are visible to the naked eye. A $10\ \mu\text{m}$ step size was used to scan the mouse ear within the $7 \times 8\ \text{mm}^2$ area of the photograph and the imaging result was shown in Fig. 5(b). The MAP image displayed not only those few large aortic vessels, but also a very rich and fine capillary network that was not visible to the naked eye in the photograph, and the morphology of the microvascular structure was clearly presented. Figure 5(c) shows a close-up MAP image in the area marked by a box in (b) and (a), and the deeper capillary network in the image was also imaged with good contrast. A pair of entangled concomitant venules and arteriole can also be clearly distinguished, as marked by the arrows in Fig. 5(c). The experimental results demonstrate that our PAM system was able to image the *in vivo* microvasculature with high resolution.

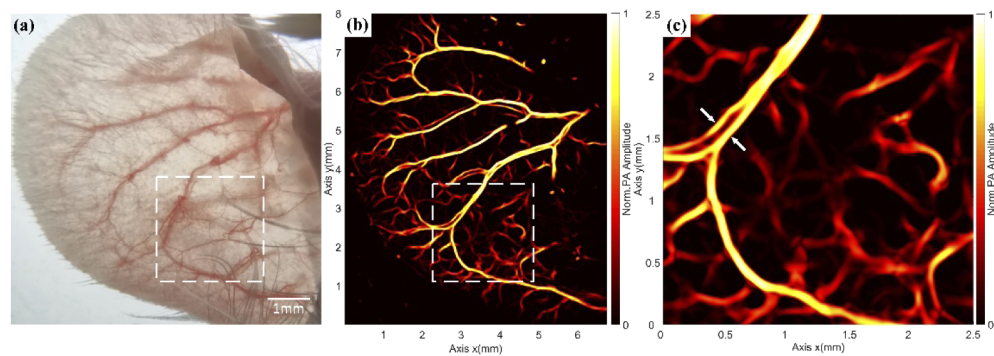


Fig. 5. (a) Photograph of the *in vivo* mouse ear. (b) MAP image of *in vivo* subcutaneous microvasculature networks of the mouse ear. (c) The close-up MAP image in the area indicated by a box in (b).

Next, we performed imaging experiments on a large area of *in vivo* subcutaneous microvascular network in the abdomen of a mouse (BALB/c-Nude). The mouse was obtained from the Laboratory Animal Research Center of Guangzhou Medical University, and the experiments were approved by the Laboratory Animal Ethics Committee. Before imaging, the mouse was anesthetized by intraperitoneal injection of a suitable amount of chloralhydrate. Then the mouse abdomen was coated with ultrasound coupling agent and affixed to the polyethylene film of the imaging window. The photograph of the mouse abdomen was shown in Fig. 6(a). The white box marked area in the Fig. 6(a) was the selected imaging area with a size of $18 \times 18\ \text{mm}^2$, and its close-up photograph was shown in Fig. 6(b). It can be seen that the blood vessels in the imaging area are hardly visible with the naked eye. Setting the scan step size of $20\ \mu\text{m}$ to scan the imaging area and the acquired MAP image was shown in Fig. 6(c). The MAP image demonstrated a large area of *in vivo* subcutaneous microvascular network, with two main blood vessels crossing the entire image and their further complicated and detailed branches can also be clearly distinguished. Some of the deeper capillaries in the center region of the image can also be visualized. The absence of signal in the white boxed area in the MAP image was due to the transducer metal electrode. In the future, we will adopt ring electrodes to reduce its blocking effect on imaging. The experimental results validate our PAM system's ability to image subcutaneous capillaries at a centimeter scale with high resolution and contrast. In the biological tissue imaging experiments, the pulse energy after the galvanometer was measured to be $\sim 7\ \mu\text{J}$. Assuming the optical focus was set to be 1 mm below the surface of the sample, the laser exposure was estimated to be about

10.77 mJ/cm², which was below the American National Standards Institute (ANSI) safety skin maximum permissible exposure (MPE) limit of 22 mJ/cm².

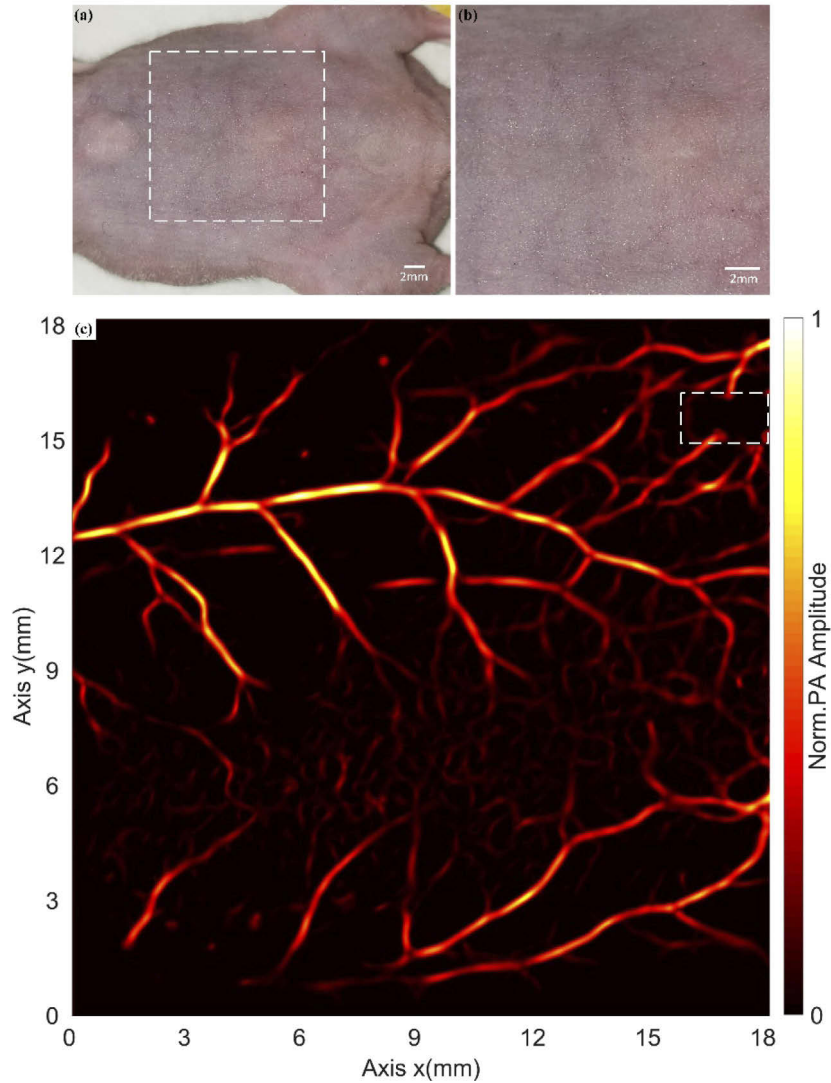


Fig. 6. (a) Photograph of the mouse abdomen. (b) Close-up photograph of the selected imaging area. (c) MAP image of the large-scale *in vivo* subcutaneous microvascular network in the mouse abdomen with 18 × 18 mm² area.

4. Discussion and conclusion

The center frequency of the transparent ultrasound transducer is inversely related to the thickness of the LiNbO₃ wafer [45]. Due to the high brittleness of LiNbO₃ material, the difficulty of fabricating same thickness LiNbO₃ wafers increases rapidly as the size increases. Therefore, it has an engineering difficulty to fabricate a transparent ultrasound transducer with both several tens of millimeters size and several tens of MHz center frequency. S. Park and H. Chen et al. have fabricated transparent ultrasound transducers with 11.2 MHz and 13 MHz center frequencies, and their wafer sizes were 7 × 7 mm² and 10 × 10 mm², respectively [36,37]. R. Chen et al.

have developed a transparent ultrasound transducer with a center frequency of up to 37 MHz and a wafer thickness of 100 μm , but the wafer size was still limited to $10 \times 10 \text{ mm}^2$. Here, we increased the LiNbO_3 wafer size to $20 \times 20 \text{ mm}^2$, with a thickness of 365 μm and a center frequency of 10 MHz. Next, it can be improved to fabricate a centimeter-scale size transparent ultrasound transducer with tens of MHz center frequency.

For large tissues and organs, photoacoustic computed tomography (PACT) is the dominant photoacoustic imaging method with a lateral resolution limited to hundreds of micrometers [46]. For example, Wray et al. achieved a maximum in-plane resolution of 255 μm by performing PACT imaging of vascular anatomy in human extremities [47]. Brecht et al. used their PACT system to generate images of whole-mouse-body with spatial resolution of approximately 500 μm [47]. In addition, PACT systems typically required a hundreds-channel data acquisition system to provide simultaneous one-to-one mapped association with the transducer array, resulting in a huge challenge of economy, complexity, and reliability [47–50]. Now, we offer a simple alternative of being higher resolution and lower cost, and the imaging FOV can be further improved to tens or even hundreds of millimeters in the future. The FOV of our system is related to the size of the transparent transducer. The limitation to the size of the transparent transducer lies in the processing technology of the LiNbO_3 wafer and the growth limit of LiNbO_3 crystals. Currently the growth limit of the LiNbO_3 crystals is about 150 mm, which is the maximum size that can be achieved for the transparent transducer. At present, the size of our transparent transducer is still far from its limit size, and we will continue to improve the processing and fabrication technology of LiNbO_3 wafer to further increase the size of the transparent transducer.

It takes about 2 minutes to acquire Fig. 5(b) and about 3 minutes to acquire Fig. 6(c) without considering signal averaging. To further increase the imaging speed of the system, in addition to using a higher repetition frequency laser, we also consider to array the transparent ultrasound transducer by referring to the approach of micro-lens array [51–54]. The first solution is placed on the back of the transparent transducer, and the laser passes through the micro-lens array to form multiple optical focus, which can greatly shorten the time for the system to acquire a photoacoustic image. The second solution is to process the transparent transducer directly into an array transducer with multiple elements by etching and other processes, which can improve the imaging signal-to-noise ratio and three-dimensional imaging capability of the PAM system. Table 1 shows the comparison of our PAM and recent PAMs in terms of imaging speed and FOV.

Table 1. Comparison of our PAM and recent PAMs in terms of imaging speed and FOV

PAMs	Imaging speed	FOV
Traditional mechanical scanning PAM [36]	1 Hz over 1 mm	> 10 mm
Voice-coil scanning PAM [29]	40 Hz over 1 mm	$\leq 9 \text{ mm}$
Optical Scanning PAM with focused transducer [26]	1800Hz over 0.1 mm	$\leq 0.1 \text{ mm}$
MEMS scanning PAM [31]	400 Hz over 3 mm	$\leq 3 \text{ mm}$
Our laser-scanning PAM with transparent transducer	100 Hz over 1 mm	$\geq 20 \text{ mm}$

In summary, in this study, we demonstrated a simple and compact PAM with a large-size transparent ultrasound transducer, which overcomes the trade-offs between imaging speed and FOV in current PAMs and achieves fast imaging over a centimeter-scale range with a lateral resolution of 17.5 μm . The imaging experiments of ink capillary and leaf vein skeleton measured the maximum imaging FOV of the PAM system was $20 \times 20 \text{ mm}^2$, and the FOV was limited only by the window size of the transparent ultrasound transducer. The imaging experiments on the mouse ear and abdomen demonstrated the PAM system's ability to resolve a large area of the subcutaneous capillary network *in vivo*. The method can simultaneously provide high imaging speed and FOV, which means it could find potentially broad applications in imaging diagnosis for

injuries and diseases of large tissues and organs [55–57], such as skin tumors, cerebral cortical tumors, diseased skin tissue of nevus flammeus and burned skin tissue.

Funding. Guangdong Province Introduction of Innovative R&D Team (2016ZT06G375); National Natural Science Foundation of China (11664011, 11804059, 51805097, 51975131); Natural Science Foundation of Jiangxi Province (20171ACB20027); The 2017 Hongcheng Plan of Nanchang Yangshen Electronic Technologies Co., Ltd.

Disclosures. The authors declare no conflicts of interest.

Data availability. No data were generated or analyzed in the presented research.

References

1. K. Maslov, H. F. Zhang, S. Hu, and L. V. Wang, "Optical-resolution photoacoustic microscopy for in vivo imaging of single capillaries," *Opt. Lett.* **33**(9), 929–931 (2008).
2. L. V. Wang, "Multiscale photoacoustic microscopy and computed tomography," *Nat. Photonics* **3**(9), 503–509 (2009).
3. P. Beard, "Biomedical photoacoustic imaging," *Interface Focus* **1**(4), 602–631 (2011).
4. S. Hu and L. V. Wang, "Photoacoustic imaging and characterization of the microvasculature," *J. Biomed. Opt.* **15**(1), 011101 (2010).
5. C. P. Favazza, O. Jassim, L. A. Cornelius, and L. H. V. Wang, "In vivo photoacoustic microscopy of human cutaneous microvasculature and a nevus," *J. Biomed. Opt.* **16**(1), 016015 (2011).
6. L. J. Rich and M. Seshadri, "Photoacoustic imaging of vascular hemodynamics: validation with blood oxygenation level-dependent MR imaging," *Radiology* **275**(1), 110–118 (2015).
7. J. Laufer, P. Johnson, E. Zhang, B. Treeby, B. Cox, B. Pedley, and P. Beard, "In vivo preclinical photoacoustic imaging of tumor vasculature development and therapy," *J. Biomed. Opt.* **17**(5), 1 (2012).
8. L. Xi, S. R. Grobmyer, L. Wu, R. M. Chen, G. Y. Zhou, L. G. Gutwein, J. J. Sun, W. J. Liao, Q. F. Zhou, H. K. Xie, and H. B. Jiang, "Evaluation of breast tumor margins in vivo with intraoperative photoacoustic imaging," *Opt. Express* **20**(8), 8726–8731 (2012).
9. Y. Zhou, W. X. Xing, K. I. Maslov, L. A. Cornelius, and L. H. V. Wang, "Handheld photoacoustic microscopy to detect melanoma depth in vivo," *Opt. Lett.* **39**(16), 4731–4734 (2014).
10. S. Jiao, M. Jiang, J. Hu, A. Fawzi, Q. Zhou, K. K. Shung, C. A. Puliafito, and H. F. Zhang, "Photoacoustic ophthalmoscopy for in vivo retinal imaging," *Opt. Express* **18**(4), 3967–3972 (2010).
11. R. H. Silverman, F. T. Kong, Y. C. Chen, H. O. Lloyd, H. H. Kim, J. M. Cannata, K. K. Shung, and D. J. Coleman, "High-resolution photoacoustic imaging of ocular tissues," *Ultrasound Med. Biol.* **36**(5), 733–742 (2010).
12. S. Jeon, H. B. Song, J. Kim, B. J. Lee, R. Managuli, J. H. Kim, J. H. Kim, and C. Kim, "In vivo photoacoustic imaging of anterior ocular vasculature: a random sample consensus approach," *Sci. Rep.* **7**(1), 4318 (2017).
13. Z. Xie, L. V. Wang, and H. F. Zhang, "Optical fluence distribution study in tissue in dark-field confocal photoacoustic microscopy using a modified Monte Carlo convolution method," *Appl. Opt.* **48**(17), 3204–3211 (2009).
14. W. Xing, L. Wang, K. Maslov, and L. V. Wang, "Integrated optical- and acoustic-resolution photoacoustic microscopy based on an optical fiber bundle," *Opt. Lett.* **38**(1), 52–54 (2013).
15. X. D. Leng, W. Chapman, B. Rao, S. Nandy, and R. Chen, "Feasibility of co-registered ultrasound and acoustic-resolution photoacoustic imaging of human colorectal cancer," *Biomed. Opt. Express* **9**(11), 5159–5172 (2018).
16. L. Zeng, G. Liu, D. Yang, and X. Ji, "Portable optical-resolution photoacoustic microscopy with a pulsed laser diode excitation," *Appl. Phys. Lett.* **102**(5), 053704 (2013).
17. L. Zeng, G. Liu, D. Yang, and X. Ji, "Cost-efficient laser-diode-induced optical-resolution photoacoustic microscopy for two-dimensional/three-dimensional biomedical imaging," *J. Biomed. Opt.* **19**(7), 076017 (2014).
18. Z. X. Xie, S. L. Jiao, H. F. Zhang, and C. A. Puliafito, "Laser-scanning optical-resolution photoacoustic microscopy," *Opt. Lett.* **34**(12), 1771–1773 (2009).
19. K. Maslov, G. Stoica, and L. H. V. Wang, "In vivo dark-field reflection-mode photoacoustic microscopy," *Opt. Lett.* **30**(6), 625–627 (2005).
20. H. F. Zhang, K. Maslov, G. Stoica, and L. H. V. Wang, "Functional photoacoustic microscopy for high-resolution and noninvasive in vivo imaging," *Nat. Biotechnol.* **24**(7), 848–851 (2006).
21. J. W. Baik, J. Y. Kim, S. Cho, S. Choi, J. Kim, and C. Kim, "Super Wide-Field Photoacoustic Microscopy of Animals and Humans In Vivo," *IEEE Trans. Med. Imaging* **39**(4), 975–984 (2020).
22. S. Hu, K. Maslov, and L. V. Wang, "Second-generation optical-resolution photoacoustic microscopy with improved sensitivity and speed," *Opt. Lett.* **36**(7), 1134–1136 (2011).
23. L. Wang, K. Maslov, and L. V. Wang, "Single-cell label-free photoacoustic flowoxigraphy in vivo," *Proc. Natl. Acad. Sci. U. S. A.* **110**(15), 5759–5764 (2013).
24. H. Estrada, J. Turner, M. Kneipp, and D. Razansky, "Real-time optoacoustic brain microscopy with hybrid optical and acoustic resolution," *Laser Phys. Lett.* **11**(4), 045601 (2014).
25. H. Wang, X. Yang, Y. Liu, B. Jiang, and Q. Luo, "Reflection-mode optical-resolution photoacoustic microscopy based on a reflective objective," *Opt. Express* **21**(20), 24210–24218 (2013).
26. P. Hajireza, W. Shi, and R. J. Zemp, "Label-free in vivo fiber-based optical-resolution photoacoustic microscopy," *Opt. Lett.* **36**(20), 4107–4109 (2011).

27. B. Rao, K. Maslov, A. Danielli, R. Chen, K. K. Shung, Q. Zhou, and L. V. Wang, "Real-time four-dimensional optical-resolution photoacoustic microscopy with Au nanoparticle-assisted subdiffraction-limit resolution," *Opt. Lett.* **36**(7), 1137–1139 (2011).
28. T. Harrison, J. C. Ranasinghesagara, H. Lu, K. Mathewson, A. Walsh, and R. J. Zemp, "Combined photoacoustic and ultrasound biomicroscopy," *Opt. Express* **17**(24), 22041–22046 (2009).
29. L. Wang, K. Maslov, J. Yao, B. Rao, and L. V. Wang, "Fast voice-coil scanning optical-resolution photoacoustic microscopy," *Opt. Lett.* **36**(2), 139–141 (2011).
30. L. Wang, K. Maslov, W. Xing, A. Garcia-Urbe, and L. V. Wang, "Video-rate functional photoacoustic microscopy at depths," *J. Biomed. Opt.* **17**(10), 1 (2012).
31. J. Yao, C.-H. Huang, L. Wang, J.-M. Yang, L. Gao, K. I. Maslov, J. Zou, and L. V. Wang, "Wide-field fast-scanning photoacoustic microscopy based on a water-immersible MEMS scanning mirror," *J. Biomed. Opt.* **17**(8), 1 (2012).
32. C. Zhang, H. Zhao, S. Xu, N. Chen, K. Li, X. Jiang, L. Liu, Z. Liu, L. Wang, and K. Wong, "Multiscale high-speed photoacoustic microscopy based on free-space light transmission and a MEMS scanning mirror," *Opt. Lett.* **45**(15), 4312–4315 (2020).
33. K. Nagae, Y. Asao, Y. Sudo, N. Murayama, Y. Tanaka, K. Ohira, Y. Ishida, A. Otsuka, Y. Matsumoto, S. Saito, M. Furu, K. Murata, H. Sekiguchi, M. Kataoka, A. Yoshikawa, T. Ishii, K. Togashi, T. Shiina, K. Kabashima, M. Toi, and T. Yagi, "Real-time 3D photoacoustic visualization system with a wide field of view for imaging human limbs," *F1000Research* **7**, 1813 (2018).
34. T. T. W. Wong, R. Zhang, P. Hai, C. Zhang, M. A. Pleitez, R. L. Aft, D. V. Novack, and L. V. Wang, "Fast label-free multilayered histology-like imaging of human breast cancer by photoacoustic microscopy," *Sci. Adv.* **3**(5), e1602168 (2017).
35. P. Zhang, L. Li, L. Lin, P. Hu, J. Shi, Y. He, L. Zhu, Y. Zhou, and L. V. Wang, "High-resolution deep functional imaging of the whole mouse brain by photoacoustic computed tomography in vivo," *J. Biophotonics* **11**(1), e201700024 (2018).
36. S. Park, S. Kang, and J. H. Chang, "Optically transparent focused transducers for combined photoacoustic and ultrasound microscopy," *J. Med. Biol. Eng.* **40**(5), 707–718 (2020).
37. H. Chen, S. Agrawal, A. Dangi, C. Wible, M. Osman, L. Abune, H. Jia, R. Rossi, Y. Wang, and S.-R. Kothapalli, "Optical-resolution photoacoustic microscopy using transparent ultrasound transducer," *Sensors* **19**(24), 5470 (2019).
38. A. Dangi, S. Agrawal, and S.-R. Kothapalli, "Lithium niobate-based transparent ultrasound transducers for photoacoustic imaging," *Opt. Lett.* **44**(21), 5326–5329 (2019).
39. J. Park, B. Park, T. Y. Kim, S. Jung, W. J. Choi, J. Ahn, D. H. Yoon, J. Kim, S. Jeon, D. Lee, U. Yong, J. Jang, W. J. Kim, H. K. Kim, U. Jeong, H. H. Kim, and C. Kim, "Quadruple ultrasound, photoacoustic, optical coherence, and fluorescence fusion imaging with a transparent ultrasound transducer," *Proc. Natl. Acad. Sci.* **118**(11), e1920879118 (2021).
40. R. Chen, Y. He, J. Shi, C. Yung, J. Hwang, L. V. Wang, and Q. Zhou, "Transparent high-frequency ultrasonic transducer for photoacoustic microscopy application," *IEEE Trans. Ultrason., Ferroelect., Freq. Contr.* **67**(9), 1848–1853 (2020).
41. A. Baba, C. T. Searfass, and B. R. Tittmann, "High temperature ultrasonic transducer up to 1000 degrees C using lithium niobate single crystal," *Appl. Phys. Lett.* **97**(23), 232901 (2010).
42. G. W. J. Brodie, Y. Qiu, S. Cochran, G. C. Spalding, and M. P. MacDonald, "Optically transparent piezoelectric transducer for ultrasonic particle manipulation," *IEEE Trans. Ultrason., Ferroelect., Freq. Contr.* **61**(3), 389–391 (2014).
43. Q. Zhou, J. H. Cha, Y. Huang, R. Zhang, W. Cao, and K. K. Shung, "Alumina/epoxy nanocomposite matching layers for high-frequency ultrasound transducer application," *IEEE Trans. Ultrason., Ferroelect., Freq. Contr.* **56**(1), 213–219 (2009).
44. Q. Zhou, S. Lau, D. Wu, and K. Shung, "Piezoelectric films for high frequency ultrasonic transducers in biomedical applications," *Prog. Mater. Sci.* **56**(2), 139–174 (2011).
45. L. M. Zeng, Z. L. Piao, S. H. Huang, W. C. Jia, and Z. P. Chen, "Label-free optical-resolution photoacoustic microscopy of superficial microvasculature using a compact visible laser diode excitation," *Opt. Express* **23**(24), 31026–31033 (2015).
46. L. V. Wang and J. Yao, "A practical guide to photoacoustic tomography in the life sciences," *Nat. Methods* **13**(8), 627–638 (2016).
47. P. Wray, L. Lin, P. Hu, and L. H. V. Wang, "Photoacoustic computed tomography of human extremities," *J. Biomed. Opt.* **24**(2), 1 (2019).
48. H. P. Brecht, R. Su, M. Fronheiser, S. A. Ermilov, A. Conjusteau, and A. A. Oraevsky, "Whole-body three-dimensional optoacoustic tomography system for small animals," *J. Biomed. Opt.* **14**(6), 064007 (2009).
49. L. Li, P. Hu, J. Shi, C. M. Appleton, M. Konstantin, L. Li, R. Zhang, and L. H. V. Wang, "Single-breath-hold photoacoustic computed tomography of the breast," *Nat. Commun.* **9**(1), 2352 (2018).
50. L. Lei, L. Zhu, M. Cheng, L. Li, J. Yao, L. Wang, K. Maslov, R. Zhang, W. Chen, and J. Shi, "Single-impulse panoramic photoacoustic computed tomography of small-animal whole-body dynamics at high spatiotemporal resolution," *Nat. Biomed. Eng.* **1**(5), 0071 (2017).
51. T. Imai, J. H. Shi, T. T. W. Wong, L. Li, L. R. Zhu, and L. H. V. Wang, "High-throughput ultraviolet photoacoustic microscopy with multifocal excitation," *J. Biomed. Opt.* **23**(3), 1 (2018).

52. J. Xia, G. Li, L. Wang, M. Nasiriavanaki, K. Maslov, J. A. Engelbach, J. R. Garbow, and L. V. Wang, "Wide-field two-dimensional multifocal optical-resolution photoacoustic-computed microscopy," *Opt. Lett.* **38**(24), 5236–5239 (2013).
53. L. Song, K. Maslov, and L. V. Wang, "Multifocal optical-resolution photoacoustic microscopy in vivo," *Opt. Lett.* **36**(7), 1236–1238 (2011).
54. G. Li, K. Maslov, and L. V. Wang, "Reflection-mode multifocal optical-resolution photoacoustic microscopy," *J. Biomed. Opt.* **18**(3), 1 (2013).
55. Y. Liu, Y. Yang, M. Sun, M. Cui, Y. Fu, Y. Lin, Z. Li, and L. Nie, "Highly specific noninvasive photoacoustic and positron emission tomography of brain plaque with functionalized croconium dye labeled by a radiotracer," *Chem. Sci.* **8**(4), 2710–2716 (2017).
56. W. Huang, R. Chen, Y. Peng, F. Duan, and L. Nie, "In Vivo quantitative photoacoustic diagnosis of gastric and intestinal dysfunctions with a broad pH-responsive sensor," *ACS Nano* **13**(8), 9561–9570 (2019).
57. Q. Yu, S. Huang, Z. Wu, J. Zheng, and L. Nie, "Label-free visualization of early cancer hepatic micrometastasis and intraoperative image-guided surgery by photoacoustic imaging," *J. Nucl. Med.* **61**(7), 1079–1085 (2020).